Tailoring the selectivity of ultralow-power heterojunction gas sensors by noble metal nanoparticle functionalization

Oleg Lupan [a,b,c,d,*], Nicolai Ababii [b], David Santos-Carballal [e,*], Maik-Ivo Terasa [a], Nicolae Magariu [b], Dario Zappa [f], Elisabetta Comini [f], Thierry Pauporte [c], Leonard Siebert [a], Franz Faupel [g,*], Alexander Vahl [g,*], Sandra Hansen [a,*], Nora H. de Leeuw [e,h], and Rainer Adelung [a,*]

[a] *Functional Nanomaterials, Faculty of Engineering, Institute for Materials Science, Kiel University, Kaiserstr. 2, D-24143, Kiel, Germany*
[b] *Center for Nanotechnology and Nanosensors, Department of Microelectronics and Biomedical Engineering, Technical University of Moldova, 168 Stefan cel Mare Av., MD-2004 Chisinau, Republic of Moldova*
[c] *PSL Université, Institut de Recherche de Chimie Paris-IRCP, Chimie ParisTech, rue Pierre et Marie Curie 11, 75231 Paris Cedex 05, France*
[d] *Department of Physics, University of Central Florida, Orlando, FL 32816-2385, USA*
[e] *School of Chemistry, University of Leeds, Leeds LS2 9JT, United Kingdom*
[f] *Sensor Laboratory, Department of Information Engineering (DII), University of Brescia, Via Branze 38, Brescia 25123, Italy*
[g] *Chair for Multicomponent Materials, Faculty of Engineering, Kiel University, Kaiserstr. 2, D-24143, Kiel, Germany*
[h] *Department of Earth Sciences, Utrecht University, Princetonplein 8A, 3584 CD Utrecht, The Netherlands*

*Corresponding authors:
Rainer Adelung (ra@tf.uni-kiel.de),
Oleg Lupan (ollu@tf.uni-kiel.de , oleg.lupan@mib.utm.md), Dr. David Santos-Carballal (d.santos-carballal@leeds.ac.uk) Dr. Alexander Vahl (alva@tf.uni-kiel.de), Dr. Sandra Hansen (sn@tf.uni-kiel.de)

1

2

Abstract

Heterojunctions are used in solar cells and optoelectronics applications owing to their excellent electrical and structural properties. Recently, these energy-efficient systems have also been employed as sensors to distinguish between individual gases within mixtures. Through a simple and versatile functionalization approach using noble metal nanoparticles, the sensing properties of heterojunctions can be controlled at the nanoscopic scale. This work reports the nanoparticle surface functionalization of $TiO_2/CuO/Cu_2O$ mixed oxide heterostructures, where the gas sensing selectivity of the material is tuned to achieve versatile sensors with ultra-low power consumption. Functionalization with Ag or AgPt-nanoclusters (5-15 nm diameter), changed the selectivity from ethanol to butanol vapour, whereas Pd-nanocluster functionalization shifts the selectivity from the alcohols to hydrogen. The fabricated sensors show excellent low power consumption below 1 nW. To gain insight into the selectivity mechanism, density functional theory (DFT) calculations have been carried out to simulate the adsorption of H_2, C_2H_5OH and n-C_4H_9OH at the noble metal nanoparticle decorated ternary heterostructure interface. These calculations also show a decrease in the work function by ~2.6 eV with respect to the pristine ternary heterojunctions. This work lays the foundation for the production of a highly versatile array of sensors of ultra-low power consumption with applications for the detection of individual gases in a mixture.

3

1. Introduction

Tuning the properties of semiconductor-powered devices by means of functional oxide nanomaterials is a state-of-the-art technological approach. Heterojunctions have gained attention for applications in optoelectronics and solar cells, but they can also be employed as versatile and ultra-low power gas sensors owning to the high degree of phase control at the nanoscopic level [1–6]. Previous studies on the decoration of semiconducting metal oxide nanostructures with nanoparticles (NPs), have demonstrated the versatile nature of such combined systems, e.g. in gas, UV and temperature sensors or for the discrimination of volatiles [7–9]. For example, a significant increase in sensitivity by a factor of ~ 60 and selectivity towards 200 ppm of ethanol vapors was achieved following surface functionalization of columnar ZnO:Fe films using AgO/Ag nanoparticles [4]. This behavior was confirmed by quantum mechanical calculations showing that $(AgO)_5$ clusters change the surface chemistry of the Fe-doped zinc oxide ZnO (10-10) surface towards ethanol detection [4]. Wang *et al*. [10] found that tetragonal rutile SnO_2 nanosheets decorated with an optimum amount of 3 mol% of NiO nanoparticles increases by five times the response to 100 ppm of C_2H_5OH at 260 °C, compared to the sensor containing only pure SnO_2 nanosheets. These findings were assigned to the formation of a *p–n* junction between the NiO nanoparticles and SnO_2 nanosheets [10]. Moreover, surface functionalisation using nanoparticles of noble metals and their alloys has been used previously to fabricate sensors for the detection of VOC molecules [9,11]. Nanometer-sized titanium dioxide (TiO_2) quantum dots (QDs) have been grown by Liu and co-workers, who found that Ag decoration led to a 6-fold increase in the sensing response toward 10–100 ppm NH_3 gas at room temperature [12]. Moreover, Wu *et al*. [13] found that for in-situ electrochemical activation through surface/interface modulation and enhancement of the catalytic performances of nanomaterials, novel bi-functional sandwich-like electrocatalysts of $FeCo_2O_4@FeCo_2S_4@PPy$ or $MCo_2O_4@MCo_2S_4@PPy$ can be used, which reveals that the bi-product interface can motivate more active sites than a single nanomaterials interface [13–16].

Some advantages of noble metal modified nanoparticles compared with pure precious metal catalysts are: the deposition time of nanoparticles is relatively small, the density of

4

nanoparticles can be directed solely by the deposition time, and no precursor solutions need to be prepared.

An excellent example for the requirement of reliable gas sensors is *n*-butanol, which is a stimulating and narcotic volatile compound, used extensively as a solvent and extracting agent of organic synthesis intermediates [17]. However, exposure to *n*-butanol vapours has adverse health effects in humans, causing symptoms including dizziness, headaches, somnolence and dermatitis [7,17,18]. The traditional and most frequently used method for the detection of *n*-butanol is gas chromatography (GC) [17,19,20], which is a complicated, time-consuming and costly technique. The current trend of developing solid state gas sensors of low energy consumption, has led to the use of metal oxide semiconductors as good candidates to fabricate highly sensitive, selective and reliable *n*-butanol gas sensors [4,17,21].

Given that one of the important advantages to improve the highly selective sensitivity for certain specific gases and VOCs is the functionalization of the nanostructured semiconducting metal oxide surfaces with different types of noble metals [6], this study reports the fabrication of gas sensors for VOCs and H_2 using a titania/cupric oxide/cuprite (TiO_2/CuO/Cu_2O/glass) heterostructure decorated with noble metal nanoparticles. To gain insight into the sensing mechanism, we also present calculations based on the density functional theory (DFT) of the ternary heterojunction $TiO_2(111)$/CuO$(\bar{1}11)$/$Cu_2O(111)$ decorated with Pd_7, Ag_7 and Ag_6Pt nanoparticles, where we have calculated the adsorption energies, structures and work functions after impregnation with the noble metal nanoclusters. Despite the lattice mismatch introduced by the deposition of the monoclinic CuO$(\bar{1}11)$ and $TiO_2(111)$ thin film overlayers on the $Cu_2O(111)$ substrate surface with hexagonal symmetry, this is a thermodynamically stable heterostructure [22,23]. The change of selectivity of the sensors is investigated by examining the binding energies and charge transfers for the interactions of molecular hydrogen (H_2), ethanol (C_2H_5OH) and *n*-butanol (*n*-C_4H_9OH) with the heteroepitaxial junctions functionalized by the noble metal nanoparticles.

This work demonstrates that the introduction of noble metal nanoparticles on the surface of TiO_2/CuO/Cu_2O presents a suitable route towards developing gas sensing devices with

5

ultra-low energy consumption. The nanoscopic scale of the functionalisation also allows tuning, modulating and controlling the selectivity and response of these sensors, which can be used for practical applications requiring the discrimination between different VOCs and H_2 gas.

2. Material and methods

2.1. Experimental

Synthesis of the CuO-Cu$_2$O ultra-thin layers (20-60 nm of thickness) was achieved by sputtering a thin film of copper metal (Cu film with 20, 30, 40, 50 and 60 nm thicknesses) on top of a clean glass under vacuum conditions. The glass samples coated with the thin film of copper metal were thermally treated at 420°C in an electrical furnace for 30 or 60 min under normal ambient conditions, because in the range of temperatures between 350 and 450°C the mixed CuO/Cu$_2$O crystal phases are formed [22,24], which are well above the operating temperature (250°C and 350°C) used for our sensing measurements, ensuring that CuO is not transformed into the Cu$_2$O phase or vice versa during the sensing process. Next, titania (TiO$_2$) films of 20 nm thick were spray-deposited on top of the layers of the mixed copper oxide phases, thus preparing six additional sample sets. Afterwards, the samples of the TiO$_2$/CuO/Cu$_2$O heterostructure were treated in air at 420°C for another 30 min (for the Cu20, Cu30, Cu40 samples) or 60 min (for the Cu50, Cu60 samples), depending on their thickness, before allowing them to cool down to room temperature. The next step comprised the sputtering of Au top-contacts on the surface of the fabricated TiO$_2$/CuO/Cu$_2$O samples by means of a meander-shaped mask. The TiO$_2$/CuO/Cu$_2$O thin films were decorated with Ag and AgPt alloy nanoparticles (Ag NP and AgPt NP) using a high vacuum deposition system (custom-made) with attached Gas Aggregation Source (GAS, Haberland type [25]). Details of the deposition of noble metal alloy nanoparticles can be found in our earlier work [7,26]. For the preparation of thin film composites with Pd NPs, a similar custom-constructed chamber for deposition under high vacuum and with attached Haberland-type GAS was used [9,11,27] following the technological approach developed by Lupan et al. [28].

A TiO$_2$/CuO/Cu$_2$O nanocomposite thin film, decorated with AgPt NPs, was investigated using X-ray photoelectron spectroscopy (XPS, Omicron Nano-Technology GmbH, Al, 240 W). The obtained XPS data were charge referenced with respect to aliphatic carbon C1s at 285.0 eV and analysed ("CasaXPS, version 2.3.16") [9,11,27].

7

For the electrical studies, different bias voltages were applied to the functionalized samples and measurements were taken continuously and registered using a computer-controlled Keithley2400 sourcemeter using the LabView software (National Instruments). The gas response was determined as the ratio ($\frac{R_g - R_a}{R_a} \cdot 100\%$), where R_g and R_a stand for the resistance of the device structures exposed to gas or air, accordingly [22,29].

The general technological flow process for the manufacture of the $TiO_2/CuO/Cu_2O$ heterostructure-based sensor devices, which is represented in Figure 1, consists of surface functionalization using Pd, Ag or AgPt nanoparticles. The inset of Figure 1 represents a cross-section view of the multilayered devices comprising the Pd-, Ag- or AgPt-NPs/$TiO_2/CuO/Cu_2O$ systems.
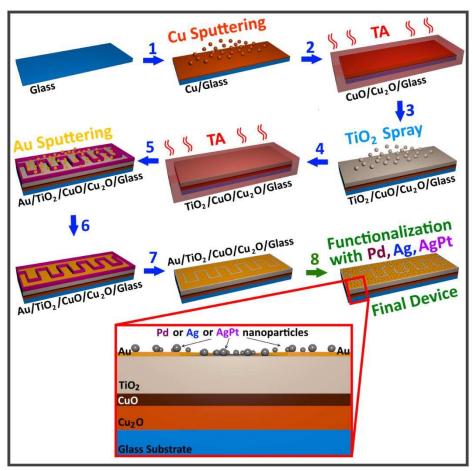

Fig. 1. The technological flowchart for the manufacture of the sensor device structures based on nanostructured layered films consisting of Pd, Ag or AgPt NPs on top of the $TiO_2/CuO/Cu_2O$ heterostructure (Final device structure). Cross-section view of a device based on Pd, Ag or AgPt NPs on top of the $TiO_2/CuO/Cu_2O$ -based sensor in the inset.

8

2.2.Computational details

We have used the Vienna Ab initio Simulation Package (VASP) [30–33] to carry out spin-polarized calculations within the usual Kohn-Sham (KS) implementation of the density functional theory (DFT). The generalized gradient approximation (GGA) was employed with the Perdew, Burke and Ernzerhof (PBE) functional for the exchange-correlation energy [34,35]. Long-range dispersion interactions were included using the semi-empirical method of Grimme, with the Becke-Johnson damping [D3-(BJ)] [36,37], which is required for the realistic simulation of the bulk and surface properties of several different materials [9,38–45]. The inner electron included up to the 3*s* level for Cu; 2*p* level for Ti; 4*f* level for Pt; 4*s* level for Pd and Ag; and 1*s* level for O, C and N, and were described by the projector augmented wave (PAW) method [46,47], whereas the electron of the H atom was treated as valence. The valence states were expanded in a periodic plane-wave basis set with a cut off at 400 eV for the kinetic energy. An energy threshold defining self-consistency of the electron density was set at 10^{-5} eV. An efficient conjugate-gradients technique based on the Newton line optimizer [48,49] was used for the relaxation of the geometries, which reached the ground state when the Hellmann-Feynman forces on all atoms were smaller than 0.01 eV·Å^{-1}. We have used the Hubbard approximation [50] in the form of the Dudarev *et al.* [51] scheme to improve the description of localized *d* states in this type of system, where the standard GGA functionals fail [52]. The values for the on-site Coulomb interaction term in this study were U_{eff} = 4.0 eV for Cu and 4.4 eV for Ti [22,23,53–57]. However, no Hubbard Hamiltonian was applied to the *d* states of the noble metal NPs, as they are already delocalised given the electron conducting properties of these materials [58,59]. These criteria allowed convergence of the total electronic energy to within 1 meV·atom^{-1}.

The electronic integrations of the face-centred cubic (*fcc*) transition metal phases were calculated in the reciprocal space using their primitive unit cells and a *Γ*-centred Monkhorst-Pack (MP) sampling grid [60] containing $17 \times 17 \times 17$ *k*-points, which was sufficient to simulate correctly their conducting electronic properties [58,59]. The

9

nanoparticle-functionalised TiO$_2$(111)/CuO ($\bar{1}$11) /Cu$_2$O(111) heterostructure was simulated using a Γ-centred MP mesh [60] of $5 \times 5 \times 1$ k-points, in line with previous works [22,23]. The isolated molecules were modelled in a cell with broken symmetry and dimensions of 20×21×22 Å^3, considering only the Γ point of the Brillouin zone. The electronic partial occupancies of the isolated molecules were determined using the Gaussian smearing method with a smearing width of 0.05 eV. The method of Methfessel-Paxton order 1 with a sigma value of $\sigma = 0.2$ eV was applied to the *fcc* metal phases [61], which ensured a negligible variational quantity, *i.e.* electronic entropy [62]. Moreover, the tetrahedron method with Blöchl corrections [63] was used for the calculation of the electronic and magnetic properties and to obtain very accurate total energies for the nanoparticle functionalised heteroepitaxial junctions before and after molecular adsorption of the gases.

3. Results and Discussion

3.1. Morphological evolutions and composition analysis

Scanning electron microscope (SEM) images are presented in Figure 2 for the mixed copper oxide CuO/Cu_2O substrate coated with a TiO_2 layer and functionalised with the Pd, Ag and AgPt noble metal nanoparticles. The surface of the $TiO_2/CuO/Cu_2O$ material is covered with nanoclusters of 5-15 nm in diameter, which are forming uniformly interconnected nano-crystallites, which is favourable for sensor device applications. The SEM images of the CuO/Cu_2O, $TiO_2/CuO/Cu_2O$ and $AgPt/TiO_2/CuO/Cu_2O$ samples are shown in Figures S1. To better understand the structures, the SEM images at high and low magnification are represented in Figures S2 and S3 in the Supporting Information.
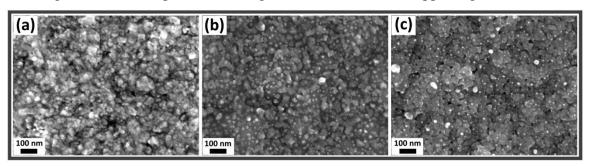

Fig. 2. Higher magnification of SEM images of interconnected $TiO_2/CuO/Cu_2O$ nano-crystallite samples covered with: (a) Pd nanoparticles, with CuO/Cu_2O thickness of 20 nm (Cu20); (b) Ag nanoparticles, with CuO/Cu_2O thickness of 60 nm (Cu60); (c) AgPt nanoparticles, with CuO/Cu_2O thickness of 60 nm (Cu60)). Noble metal nanoclusters have 5-15 nm in diameter.

3.2. X-ray photoelectron spectroscopy, Micro-Raman and UV-Visible-NIR spectroscopy characterization of CuO/Cu_2O and $TiO_2/CuO/Cu_2O$ nanocomposite

The X-ray photoelectron spectra (XPS) of the $TiO_2/CuO/Cu_2O$ nanocomposite decorated with AgPt NPs are shown in Figure 3. Cu, O, Ti, Na and C elements were detected in both the nanocomposite as well as in the $TiO_2/CuO/Cu_2O$ reference thin film, see the overview spectra in Figure 3a. The presence of Cu, O and Ti originates from the $TiO_2/CuO/Cu_2O$ base layer, although the signal from carbon is due to contamination of the top surface with C from the atmosphere, e.g. from carbohydrates [9,11,27]. The observation of the signal corresponding to Na is due to diffusion from the glass

11

substrates, which were used for the deposition of the sensor structures [7,64,65]. Such peaks were not detected from samples deposited on quartz substrates (not shown here).

Figure 3b depicts the high-resolution spectra of the Cu-2p, Ti-2p, Ag-3d and Pt-4d lines. A closer look at the Cu-2p line reveals clear satellite peaks for both the Cu-$2p_{3/2}$ and Cu-$2p_{1/2}$ lines, which are relocated to higher binding energies. The Cu-$2p_{3/2}$ line, as well as the corresponding satellites, were assigned to the nanocomposite – see deconvolution of $2p_{3/2}$ with satellite peaks into 3 subpeaks. The observed satellite peaks are generally regarded as a signature for the occurrence of the CuO/Cu_2O heterojunction with CuO exposed at the surface [8,9]. Accordingly, the signal from copper in the spectrum can be assigned to the existence of CuO/Cu_2O in the base layer.

A Ti-$2p_{3/2}$ peak in the range 459.6 eV - 458.0 eV is usually assigned to Ti^{4+} in TiO_2. The evaluation of high resolution Ti-2p XPS binding energies reveals that the Ti-$2p_{3/2}$ line is positioned around 458.3 eV. The peak positions of Ti-$2p_{3/2}$ and Ti-$2p_{1/2}$ and their separation of 5.6 eV indicate the presence of Ti in the form of TiO_2 in the base layer [66,67].

Ag and Pt were detected alongside Cu, Ti, O and C in the $TiO_2/CuO/Cu_2O$ nanocomposite decorated using the AgPt NPs. Spectra at higher resolution of the Ag-3d and Pt-4d lines were recorded in order to evaluate the composition of the AgPt NPs. We chose the Pt-4d lines for quantification due to the overlap of Pt-4f with intensive Cu-3p lines. In the case of the nanocomposite, the quantification of the AgPt NPs yields a platinum content of roughly 15 at% within the nanoparticles. A detailed investigation of AgPt NPs can be found in our earlier works [7,11].

In addition to the functionalisation of the $TiO_2/CuO/Cu_2O$ nanocomposite with AgPt NPs, we also used Pd nanoparticles [28] to prepare the decorated sensors in the context of this work. The respective overview and high-resolution spectra corresponding to the TiO_2/CuO structures with and without decoration by Pd NPs are shown in Figure S4 (Supporting Information). In general, the spectra of the AgPt nanoparticle- and Pd nanoparticle-decorated sensors show strong similarities and mostly differ in the signals corresponding to the elemental Ag, Pt or Pd. The observation of the Pd-3d lines with

12

peaks around 335.8 eV (Pd-3d$_{5/2}$) and 341.0 eV (Pd-3d$_{3/2}$) indicates the successful decoration of the sensor structure by Pd nanoparticles [28].
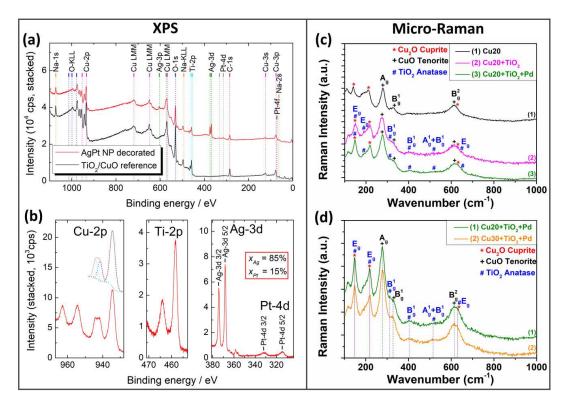

Fig. 3. X-ray photoelectron spectra (XPS) of: (a) a AgPt/TiO$_2$/CuO/Cu$_2$O (red line) nanocomposite and an undecorated TiO$_2$/CuO/Cu$_2$O thin film (black line); (b) spectra at higher resolution for Cu-2p and Ti-2p lines as well as spectra for Ag-3d and Pt-4d lines. Micro-Raman spectra for: (c) the surface functionalized TiO$_2$/CuO/Cu$_2$O and Pd/TiO$_2$/CuO/Cu$_2$O samples with CuO/Cu$_2$O thickness of 20 nm (Cu20) after being thermally treated at 420°C for 30 min in ambient; (d) Pd/TiO$_2$/CuO/Cu$_2$O with CuO/Cu$_2$O thicknesses of 20 nm (Cu20) and 30 nm (Cu30), respectively.

The micro-Raman spectra of the CuO/Cu$_2$O, TiO$_2$/CuO/Cu$_2$O and Pd/TiO$_2$/CuO/Cu$_2$O nanocomposites, which were investigated at room temperature in the range 100-1000 cm^{-1}, are shown in Figure 3c and Figure 3d. The presence of metallic Cu and Pd could not be ascertained in these materials, due to the instrumental limitations related to the measurement of their dielectric constants, which possess negative real and imaginary positive components exhibited in the surface plasmon resonance (SPR) experiments [68,69]. In the case of the metal nanoclusters, the local SPRs are pledged for the field improvement, which undergo surface-enhanced processes [68,69], that are only observed

13

when using surface-enhanced Raman spectroscopy. Only phonon frequencies of the crystalline Cu_2O, CuO and TiO_2 layers are observed with our experimental set-up, as the group theory indicates that the Raman response is a function of the space group symmetry of the crystal [70].

Figure S5 illustrate the Ultraviolet, Visible and Near InfraRed (UV-Vis-NIR) absorption spectra for the $Pd/TiO_2/CuO/Cu_2O$ heterostructures, which confirm the energy structures and optical properties of this transparent semiconducting oxide. The Tauc plots for the $Pd/TiO_2/CuO/Cu_2O$ heterostructures, presented in Figure S6, reveal a bandgap that widens with the reduction of the nanoparticle size from 30 to 10 nm. As expected, the absorption edge of 2.04 eV for the 20 nm sample is equal to the value published for bulk Cu_2O [71–74].

3.3. Gas sensing properties

Heterostructures formed by *p-n* semiconductors, especially those functionalized with noble metals have a high catalytic activity and can be used to enhance the surface reactions of chemical sensing materials [7,75]. It is known that the functionalization of oxides (such as ZnO, SnO_2, TiO_2, Cu_2O and Fe_2O_3) with different noble metals or their alloys improves significantly their sensing performance. In this section the sensing properties of the $TiO_2/CuO/Cu_2O$ heterostructure functionalized with the Pd, Ag or AgPt NPs will be discussed.

3.3.1. Gas sensing properties of Pd/TiO₂/CuO/Cu₂O heterostructures

The gas sensing characteristics of the $TiO_2/CuO/Cu_2O$ samples with CuO/Cu_2O thickness of 20 nm (Cu20) functionalized using Pd NPs ($Pd\text{-}NPs/TiO_2/CuO/Cu_2O$) were investigated towards different volatile organic compounds and hydrogen. Our main aim is to show experimentally that Pd-functionalization of such structures significantly increases the response and selectivity to hydrogen gas, even at low operating temperature. We also intend to demonstrate that it is possible to lower the energy consumption during operation

14

and tune the reactivity toward H_2 of the $TiO_2/CuO/Cu_2O$ heterojunction sensors through functionalization by Pd nanoparticles.
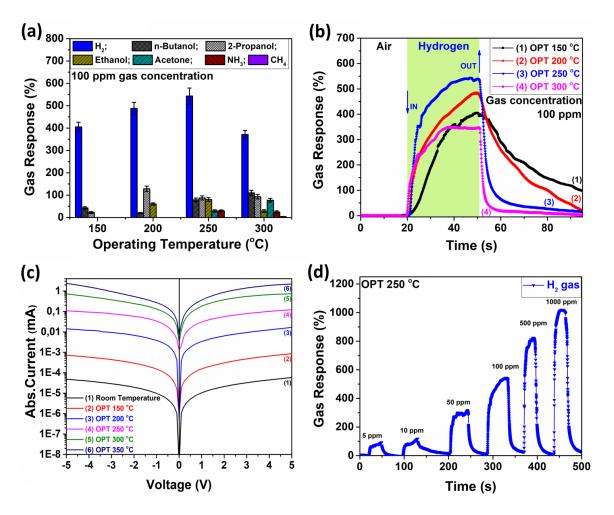

Fig. 4. (a) Gas response towards different compounds (hydrogen, *n*-butanol, 2-propanol, ethanol, acetone, ammonia and CH_4) of the Pd-functionalized $TiO_2/CuO/Cu_2O$ samples with CuO/Cu_2O thickness of 20 nm (Cu20) at different operating temperatures (OPT); (b) Dynamic response to hydrogen of the Pd/$TiO_2/CuO/Cu_2O$ samples with CuO/Cu_2O thickness of 20 nm (Cu20) measured at several OPTs; (c) The I-V current-voltage characteristics of the Pd/$TiO_2/CuO/Cu_2O$ samples with CuO/Cu_2O thickness of 20 nm (Cu20) at different OPT; (d) Dynamic response to different concentrations of hydrogen (5, 10, 50, 100, 500 and 1000 ppm) of the Pd/$TiO_2/CuO/Cu_2O$ samples with CuO/Cu_2O thickness of 20 nm (Cu20) (applied bias voltage of 250 mV).

Figure 4a shows the response versus operating temperature to hydrogen, *n*-butanol, 2-propanol, ethanol, acetone, ammonia and CH_4 by the $TiO_2/CuO/Cu_2O$ samples after surface functionalization with the Pd-NPs (for a CuO/Cu_2O specimen of 20 nm of thickness labelled as Cu20 set sample), where we observe a high and selective response

15

to H_2 at all working temperatures. The responses are ~405%, ~487%, ~543% and ~371% at the operating temperatures of 150°C, 200°C, 250°C and 300°C, respectively. The optimal operating temperature was found within the range 200-250°C. Figure 4b shows the dynamic hydrogen response of the Pd-NPs/TiO$_2$/CuO/Cu$_2$O (Cu20) samples at different operating temperatures. The calculated response times (τ_r = 18.7, 20.4, 12.8 and 12.4 s) and recovery times (t_d = (> 50), 36.3, 10.6 and 4.2 s) are relatively small at the operating temperatures of 150°C, 200°C, 250°C and 300°C, respectively, see Figure S7a. The dynamic response to different gases (hydrogen, *n*-butanol, 2-propanol, ethanol, acetone, ammonia and CH$_4$) of Pd-NPs/TiO$_2$/CuO/Cu$_2$O with CuO/Cu$_2$O thickness of 20 nm (Cu20) at an operating temperature of 250°C can be seen in Figure S7b. Figure 4c shows that the current increases with the operating temperature for the Pd/TiO$_2$/CuO/Cu$_2$O material. Figure 4d shows the dynamic response to different hydrogen concentrations (5, 10, 50, 100, 500 and 1000 ppm) of the functionalized Pd/TiO$_2$/CuO/Cu$_2$O (Cu20) samples, where a fairly high response of ~88% is registered at 5 ppm. The dynamic response to H_2 gas with concentrations of 5 and 50 ppm is presented in Figure S8.

Figure S9a presents the response to hydrogen, *n*-butanol, 2-propanol, ethanol, acetone and ammonia of the Pd/TiO$_2$/CuO/Cu$_2$O (for a substrate with CuO/Cu$_2$O thickness of 30 nm, referred as Cu30) samples, which possess the highest response towards H_2 gas (> 550%). Figure S9c displays the dynamic response to hydrogen of the Pd/TiO$_2$/CuO/Cu$_2$O (Cu30) samples at various OPTs and Figure S9d illustrates the dynamic response to hydrogen gas with three consecutive pulses at the operating temperatures 300°C. These samples clearly show superior sensing performances, which can be of major practical interest in device applications.

3.3.2. *Gas sensing properties of Ag/TiO$_2$/CuO/Cu$_2$O*

Next, the surface functionalization with the Ag nanoparticles of the TiO$_2$/CuO/Cu$_2$O samples (CuO/Cu$_2$O with thickness of 60 nm (Cu60)) was realized to tune the response to

VOCs, namely to change the selectivity from ethanol (in the case of the CuO/Cu_2O samples) to *n*-butanol.

Figure 5a shows the response to several gases versus the OPTs of the surface functionalized $Ag/TiO_2/CuO/Cu_2O$ (Cu60) samples (CuO/Cu_2O with thickness of 60 nm). We observe that, at the low operating temperatures of 200°C, the sample has *n*-type conductivity and shows sensing capabilities only towards 2-propanol and ethanol, because the electrical resistivity decreases after the molecular interactions. At the working temperatures OPTs of 250°C, 300°C and 350°C, the sample already has *p*-type conductivity and is therefore selective to *n*-butanol, where the responses are ~54%, ~200%, and ~163%, respectively. This phenomenon is dictated by the composition of the sample, which changes the surface activity and reaction products [7,22,23], by band bending and formation of electron depletion or space charge layer in the conduction band, that either decreases or increases the conductivity of the active materials [76]. The lower operating temperature does not influence the depletion layer of electrons in TiO_2, whereas the CuO/Cu_2O layer has a higher resistance, forcing currents flowing through the TiO_2 layer which is an *n*-type semiconductor. However, at higher operating temperatures the depletion layer of electrons in TiO_2 and the accumulation layer of holes in CuO/Cu_2O are also affected. As a result, the CuO/Cu_2O layer impacts the sensing mechanism, which increases the heterojunction resistance to the application of the target gas [77]. Figure 5b shows the dynamic response towards hydrogen, *n*-butanol, 2-propanol, ethanol and acetone for the $Ag/TiO_2/CuO/Cu_2O$ (Cu60) samples at the optimal OPT of 300°C.
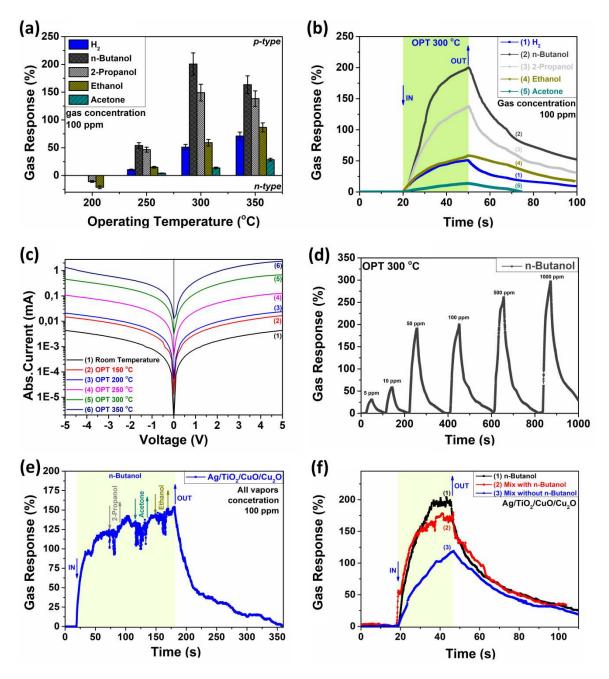
Fig. 5. (a) Gas response towards hydrogen, *n*-butanol, 2-propanol, ethanol and acetone for the TiO$_2$/CuO/Cu$_2$O samples after surface functionalization with Ag-nanoparticles (CuO/Cu$_2$O with thickness of 60 nm (Cu60)); (b) Dynamic response to different compounds (hydrogen, *n*-butanol, 2-propanol, ethanol and acetone) of the Ag/TiO$_2$/CuO/Cu$_2$O (Cu60) samples at the operating temperature of 300℃. (c) The current – voltage behavior of the Ag/TiO$_2$/CuO/Cu$_2$O (Cu60) samples at different operating temperatures; (d) Dynamic response to various concentrations of *n*-butanol (5, 10, 50, 100, 500 and 1000 ppm) of the Ag/TiO$_2$/CuO/Cu$_2$O (Cu60) samples (applied bias voltage 27.5 mV). (e) Dynamic response to 100 ppm of *n*-butanol and consecutively 2-propanol, acetone, ethanol in air of Ag/TiO$_2$/CuO/Cu$_2$O samples. (f) Dynamic response to 100 ppm of *n*-butanol and mixture of alcohols in air, with and without *n*-butanol vapors with 1000 ppm of Ag/TiO$_2$/CuO/Cu$_2$O samples.

18

Figure 5c shows the current-voltage performance of the Ag/TiO$_2$/CuO/Cu$_2$O (Cu60) samples, where the conductance increases with the operating temperature in the tested range. Figure 5d displays the dynamic response to 5, 10, 50, 100, 500 and 1000 ppm of *n*-butanol for the Ag/TiO$_2$/CuO/Cu$_2$O (Cu60) samples, demonstrating that a response of about 31% is registered even for the lowest concentration of this gas. The dynamic response to 5, 50 and 100 ppm of *n*-butanol of the Ag/TiO$_2$/CuO/Cu$_2$O samples with CuO/Cu$_2$O thickness of 60 nm (Cu60) at the operating temperature of 300°C is presented in Figure S10. Figure 5e displays the dynamic response to 100 ppm of *n*-butanol and consecutively 2-propanol, acetone, ethanol in air, of Ag/TiO$_2$/CuO/Cu$_2$O samples. Figure 5f displays the dynamic response to 100 ppm of *n*-butanol and mixtures of alcohols in air, with and without *n*-butanol vapors, with 1000 ppm of Ag/TiO$_2$/CuO/Cu$_2$O samples.

3.3.3. *Gas sensing properties of AgPt/TiO$_2$/CuO/Cu$_2$O*

Next, the response to different compounds by the AgPt/TiO$_2$/CuO/Cu$_2$O (Cu60) samples were studied at various working temperatures to investigate whether we can tune the selectivity by means of changing the composition of the NPs.
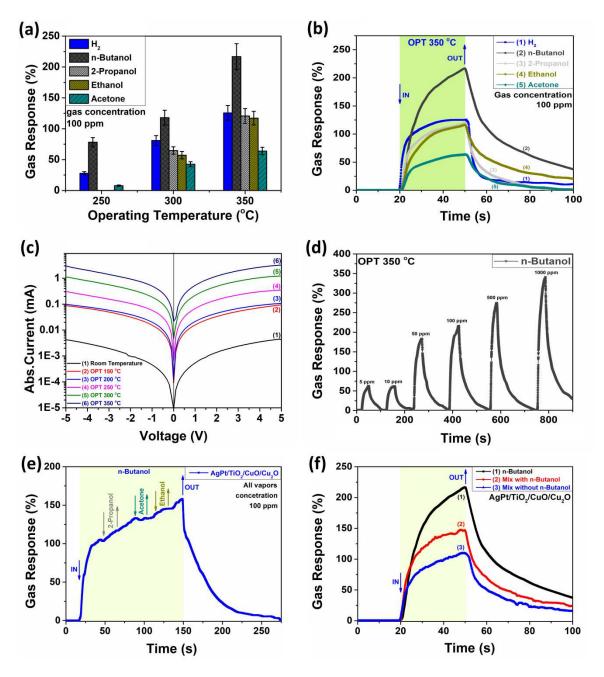
Fig. 6. (a) Gas response to different gases and volatiles (hydrogen, *n*-butanol, 2-propanol, ethanol and acetone) of the AgPt-NPs surface functionalized $TiO_2/CuO/Cu_2O$ samples with CuO/Cu_2O thickness of 60 nm (Cu60); (b) Dynamic response to hydrogen, *n*-butanol, 2-propanol, ethanol and acetone for AgPt/$TiO_2/CuO/Cu_2O$ (Cu60) samples at the operating temperature of 350°C. (c) Current-voltage characteristic of the AgPt/$TiO_2/CuO/Cu_2O$ (Cu60) samples at different operating temperatures; (d) Dynamic response to 5, 10, 50, 100, 500 and 1000 ppm of *n*-butanol of AgPt/$TiO_2/CuO/Cu_2O$ (Cu60) samples (applied bias voltage 9.5 mV). (e) Dynamic response to 100 ppm of *n*-butanol and consecutively 2-propanol, acetone, ethanol in air of AgPt/$TiO_2/CuO/Cu_2O$ samples. (f) Dynamic response to 100 ppm of *n*-butanol and mixtures of alcohols in air with and without *n*-butanol vapors with 1000 ppm of AgPt/$TiO_2/CuO/Cu_2O$ samples.

20

Figure 6a shows the response to hydrogen, *n*-butanol, 2-propanol, ethanol and acetone versus the OPT for the surface-functionalized AgPt/TiO$_2$/CuO/Cu$_2$O samples with CuO/Cu$_2$O thickness of 60 nm (Cu60). At the OPT of 250°C, 300°C and 350°C, the sample is selective to *n*-butanol and the responses are ∼78%, ∼118%, and ∼216%, respectively, suggesting that the optimal operating temperature is therefore 350°C. Figure 6b illustrate the dynamic response to hydrogen, *n*-butanol, 2-propanol, ethanol and acetone of the AgPt/TiO$_2$/CuO/Cu$_2$O (Cu60) samples at the operating temperatures of 350°C. Figure 6c illustrate the current-voltage characteristics of AgPt/TiO$_2$/CuO/Cu$_2$O (Cu60) samples, where we observe that the conductance increases with the operating temperature. Figure 6d shows the dynamic response to 5, 10, 50, 100, 500 and 1000 ppm of *n*-butanol for the Cu60 AgPt/TiO$_2$/CuO/Cu$_2$O samples with CuO/Cu$_2$O thickness of 60 nm, where a response of ∼63% is registered for 5 ppm of *n*-butanol. Figure 6e displays the dynamic response to 100 ppm of *n*-butanol and consecutively 2-propanol, acetone, ethanol in air of AgPt/TiO$_2$/CuO/Cu$_2$O samples. Figure 6f displays the dynamic response to 100 ppm of *n*-butanol and mixtures of alcohols in air with and without *n*-butanol vapors with 100 ppm of AgPt/TiO$_2$/CuO/Cu$_2$O samples. The dynamic response of the AgPt/TiO$_2$/CuO/Cu$_2$O samples (Cu60) to 5, 50 and 100 ppm of *n*-butanol at the OPT of 350°C is presented in Figure S11. Thus, chemical sensitization facilitates the adsorption of certain gas molecules on the metal NP surface, thus inducing more interactions with pre-absorbed oxygen species, facilitating relevant chemical reactions, the charge transfer, increase the electrocatalytically active surface area and therefore an improved gas detection performance [5,6].

3.3.4. *Comparison of the gas sensing properties and energy consumption of the heterostructures*

In this section, we compare the gas responses for the TiO$_2$/CuO/Cu$_2$O heterostructures functionalized with the different types of NPs-, as we aim to show the possibility of controlling their selectivity by using the technological approach developed in this work.
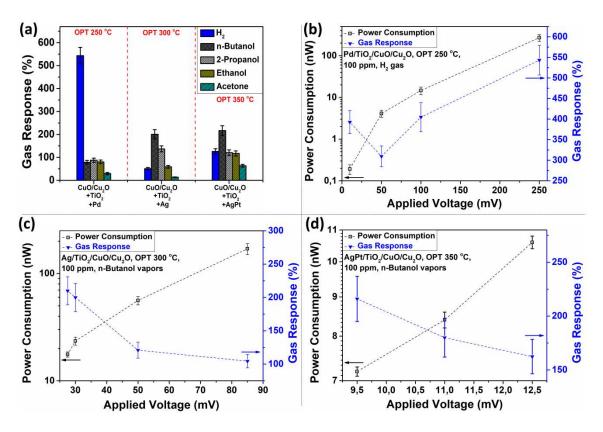
21

Fig. 7. (a) Gas response to different compounds (hydrogen, *n*-butanol, 2-propanol, ethanol and acetone) of the Pd/TiO$_2$/CuO/Cu$_2$O, Ag/TiO$_2$/CuO/Cu$_2$O, and AgPt/TiO$_2$/CuO/Cu$_2$O samples. Dependence of the power consumption and of the gas versus the applied bias voltage for: (b) Pd/TiO$_2$/CuO/Cu$_2$O (with CuO/Cu$_2$O thickness of 20 nm (Cu20)), (c) Ag/TiO$_2$/CuO/Cu$_2$O (with CuO/Cu$_2$O thickness of 60 nm (Cu60)), and (d) AgPt/TiO$_2$/CuO/Cu$_2$O (with CuO/Cu$_2$O thickness of 60 nm (Cu60)).

Figure 7a shows the gas response to hydrogen, *n*-butanol, 2-propanol, ethanol and acetone for the Pd/TiO$_2$/CuO/Cu$_2$O, Ag/TiO$_2$/CuO/Cu$_2$O, and AgPt/TiO$_2$/CuO/Cu$_2$O samples. The samples functionalized with Pd nanoparticles are the most sensitive to hydrogen, whereas the samples functionalized using the Ag and AgPt nanoparticles experience a change of selectivity and are the most sensitive to butanol.

Figure 7b represents the dependence of the power consumption and of the response to 100 ppm of H$_2$ gas versus the applied bias voltage for the Pd/TiO$_2$/CuO/Cu$_2$O samples with CuO/Cu$_2$O thickness of 20 nm (Cu20). According to the figure, both the power consumption and the response to the H$_2$ gas decreases when the applied voltage is decreased. However, we also observed that for an applied bias voltage of 10 mV the

22

response increased. The power consumption obtained is ~270, ~140, ~4.1 and ~0.19 nW, and the responses are ~588%, ~404%, ~310% and ~390%, at the applied bias voltages of 250, 100, 50 and 10 mV, respectively. The response to different gases versus the applied bias voltage for the $Pd/TiO_2/CuO/Cu_2O$ samples with CuO/Cu_2O thickness of 20 nm (Cu20) is represented in Figure S12. The dependence on the power consumption and the response to 100 ppm of *n*-butanol vapors versus applied bias voltage for $Ag/TiO_2/CuO/Cu_2O$ with CuO/Cu_2O thickness of 60 nm are represented in Figure 7c, where it can be seen that the obtained power consumption is ~170, ~56, ~23.5 and ~17.6 nW, and the respective responses are ~104%, ~121%, ~200% and ~210%, at the applied bias voltages of 85, 50, 30 and 27.5 mV, respectively. For the $AgPt/TiO_2/CuO/Cu_2O$ samples with CuO/Cu_2O thickness of 60 nm (Cu60), the power consumption is ~10.6, ~8.4 and ~7.2 nW, and the responses are ~162%, ~180% and ~216% to 100 ppm of *n*-butanol vapors at the applied bias voltages of 12.5, 11.0 and 9.5 mV, respectively, shown in Figure 7d, where it can be seen that the obtained power consumption is ~10.6 nW, ~8.4 nW and ~7.2 nW, and the respective responses are ~162%, ~180% and ~216%, at the applied voltages of 12.5 mV, 11.0 mV and 9.5 mV, respectively. The dependence on the power consumption versus the applied bias voltage is represented in Figure S13 for the $TiO_2/CuO/Cu_2O$ samples with CuO/Cu_2O thickness of 20 nm (Cu20) decorated with Pd or Ag or AgPt NPs.

The proposed gas sensing mechanism for our heterostructures after functionalization with noble metal nanoparticles is described in Text S1 (Supporting Information).

3.4. Deposition of nanoparticles: computational results

We have simulated the modification of the ternary $TiO_2(111)/CuO(\bar{1}11)/Cu_2O(111)$ heterostructure by adsorbing Pd_7, Ag_7 and Ag_6Pt nanoparticles, see Figure 8, to subsequently assess their selectivity and sensitivity towards the detection of hydrogen (H_2), ethanol (C_2H_5OH) and *n*-butanol (C_4H_9OH) vapors. The purpose of these simulations is to assist the interpretation of the trends of the gas response detected in the

23

experiments for our ternary heterojunctions functionalised using noble metal nanoparticles.
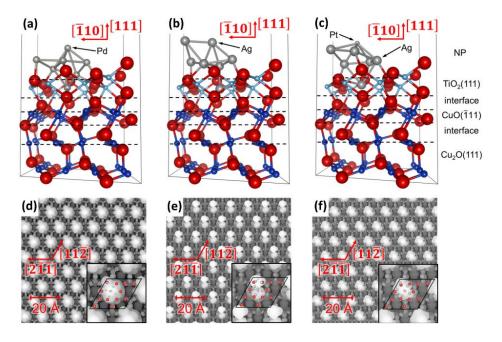

Fig. 8. (Top panels) Side view and (bottom panels) simulated scanning tunnelling microscopy (STM) images of the ternary TiO$_2$(111)/CuO($\bar{1}$11)/Cu$_2$O(111) heteroepitaxial junction functionalised using (a and d) Pd$_7$; (b and e) Ag$_7$; and (c and f) Ag$_6$Pt nanoparticles. The ternary heterojunctions functionalised using the Pd$_7$, Ag$_7$ or Ag$_6$Pt nanoparticle are displayed using the ball-and-stick representation. The STM images were generated using a bias of: (d) $V = -0.5$ eV, (e) $V = -1.0$ eV and (f) $V = -1.5$ eV, an electron density of (d) $\rho = 0.0009$ e·Å^{-3}, (e) $\rho = 0.0029$ e·Å^{-3} and (f) $\rho = 0.0070$ e·Å^{-3} as well as a tip distance of (d) $d = 2.25$ Å, (e) $d = 1.06$ Å and (f) $d = 2.17$ Å. Inset illustrate enlargement of the STM image for the surface unit cell. Crystallographic directions are indicated with respect to the Cu$_2$O(111) substrate. O atoms are in red, Cu atoms are in dark blue, Ti atoms are in light blue and Pd, Ag or Pt atoms are in grey.

The scanning tunnelling microscopy images (STM), shown in Figure 8d-f, were simulated using the HIVE code [78], which is based on the theory developed by Tersoff and Hamann [79]. The brightest spots resolved for the surface of the nanoparticle-functionalised ternary TiO$_2$(111)/CuO($\bar{1}$11)/Cu$_2$O(111) material correspond to the noble metal clusters. Figure 8d clearly shows the almost perfect 5-fold symmetry of the Pd$_7$ NP, which is only broken by the Pd atom located away from the nanoparticle axis. Following deposition, the Ag$_7$ cluster splits into conjoined twin particles, each containing three metal atoms, connected by a bridge comprising one Ag atom, as shown in Figure 8e. Figure 8f illustrates that replacing the axial and exposed Ag atom by Pt has a cohesive

24

effect in the conjoined twin particles, which reattach in a pentagon shape, although still more distorted than Pd_7. We discuss changes in the interfacial energy and work function after NP functionalisation of $TiO_2(111)/CuO\ (\bar{1}11)\ /Cu_2O(111)$ in the Supporting Information. The adsorption energies of the noble metal NPs, charge transfers and their magnetic moments are also analysed in the Text S2 (Supporting Information).

The work function of the ternary heterojunction suffers a reduction of approximately 37% from its initial large value of $\Phi = 7.454$ eV, after decoration by the noble metal nanoparticles, as listed in Table S1 and described in the Text S3 (Supporting Information). The lower work function values calculated for the hetero-devices after surface functionalisation explain their enhanced chemical reactivity, compared to the material before deposition of the metal nanoclusters. Our simulated work functions show small differences of up to 0.14 eV, suggesting that the composition of the nanoparticles can be used to fine-tune the application of the nano-composite materials as chemical sensors.

3.5. Adsorption of molecules: computational results

Here, we have modelled the surface chemistry of the ternary heteroepitaxial junction materials decorated with nanoparticles of noble metals or their alloys.

The binding energies for the interaction between the adsorbate molecules and the $TiO_2(111)/CuO\ (\bar{1}11)\ /Cu_2O(111)$ layered material functionalised with the Pd_7 nanoparticle, show a preference for H_2, releasing -1.494 eV upon interaction, see Table S2. Table S2 also lists the adsorption energies (E_{ads}) for $Ag_7/TiO_2(111)/CuO\ (\bar{1}11)\ /Cu_2O(111)$ and $Ag_6Pt/TiO_2(111)/CuO\ (\bar{1}11)\ /Cu_2O(111)$, which display a strong shift in preference towards $n\text{-}C_4H_9OH$, with calculated $E_{ads} = -1.129$ eV and -1.053 eV, respectively, on the equatorial site of the NPs. However, the adsorption of the largest molecular weight alcohol on the least coordinated axial site of the NPs leads to a reduced binding energy by around 50% compared to its equatorial Ag counterpart position. Our calculations reveal that the decreasing order of strength of molecular adsorption is $E_{ads}(n\text{-}C_4H_9OH) > E_{ads}(C_2H_5OH) > E_{ads}(H_2)$ after replacing the axial Ag atom by Pt in Ag_7, as shown in Table S2.

25

Figure 9a-c displays the thermodynamically most stable adsorption geometries for the interaction of the three molecules investigated computationally on the exposed facet of the heterostructure containing the noble metal clusters. We found that the diatomic H_2 molecule dissociates upon adsorption onto the equatorial Pd atoms of the nanoparticle, leading to the strongest interaction found in this work, see Figure 9a. For this binding mode, our calculations suggest that the H atoms place themselves approximately along the $[\bar{2}11]$ direction at either sides of the axial Pd atom. Thus, each H adatom forms a binuclear complex by coordinating both one equatorial and the axial Pd atom at the average distances of 1.71 Å and 1.78 Å. Figure S15a-c shows the binding configurations of H_2, C_2H_5OH and n-C_4H_9OH on the most favourable adsorption sites of the $Pd_7/TiO_2(111)/CuO(\bar{1}11)/Cu_2O(111)$ sensor. For the heterostructure containing the Pd_7 clusters, H_2 interacts molecularly and nearly vertically at 1.75 Å above the 5-fold axial Pd site (see Figure S15a), where it shows the least favourable adsorption observed on this material. C_2H_5OH moved outwards during the geometry optimisation from the initial equatorial site, forming a laterally coordinate bond of 2.27 Å to the axial Pd atom in its most stable adsorption configuration, as shown in Figure S15b. The O atom from the largest molecular weight alcohol stays above the initial adsorption site, *i.e.* at 2.23 and 2.13 Å from the axial and equatorial Pd sites, see Figure S14c. The Bader partition scheme reveals that H_2 lost electronic density upon adsorption, as shown in Table S2.
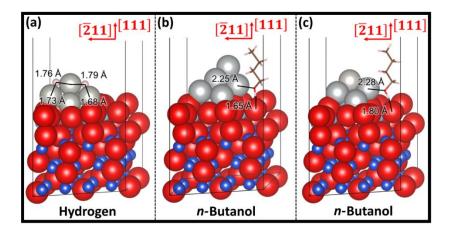

26

Fig. 9. Adsorption of: (a) H$_2$, and (b and c) n-C$_4$H$_9$OH on the TiO$_2$(111)/CuO ($\bar{1}$11) /Cu$_2$O(111) heterostructure decorated with the Pd$_7$, Ag$_7$ and Ag$_6$Pt clusters, respectively. Interatomic distances are shown and crystallographic directions are indicated with respect to the Cu$_2$O(111) substrate. The ternary heterojunctions functionalised using the Pd$_7$, Ag$_7$ or Ag$_6$Pt nanoparticles are displayed using the space-filling representation, whereas the adsorbates are shown using the stick representation. O atoms are in red, H atoms are in white, C atoms are in brown, Cu atoms are in dark blue, Ti atoms are in light blue and Pd, Ag and Pt atoms are in grey.

Figure S15d-f illustrates the binding configurations of H$_2$, C$_2$H$_5$OH and n-C$_4$H$_9$OH on the most favourable adsorption sites of the Ag$_7$/TiO$_2$(111)/CuO($\bar{1}$11)/Cu$_2$O(111) sensor. The H$_2$ molecule adorbs molecularly at approximately 2.0 Å above the axial and to the side of the equatorial sites of the Ag$_7$ nanocluster, see Figure S15d. The sensor can only exert a minor effect on the intramolecular H−H distance, with respect to the isolated H$_2$ molecule, which was calculated at 0.79 Å in both types of adsorption positions. We found that the C$_2$H$_5$OH molecule forms a vertical coordinate bond on the axial site with an O−Ag distance of 2.35 Å, which becomes 0.03 Å shorter on the equatorial adsorption position, as shown in Figure S15e. Interestingly, n-C$_4$H$_9$OH moves laterally towards a surface O to form a hydrogen bond of 1.65 Å, resulting in the shortest O−Ag distance of 2.25 Å, which explains the largest binding energy calculated for this system in the equatorial site, see Figure 9b. However, the largest molecular weight alcohol, n-butanol, interacts perpendicularly with the axial Ag atom at the slightly elongated distance of 2.31 Å. We observed that C$_2$H$_5$OH (n-C$_4$H$_9$OH) forms a vertical adsorption configuration on the heterostructure decorated using the Ag$_7$ nanoparticles.

For the molecular adsorptions on the sensor decorated by the Ag$_7$ nanoparticles, the Bader charge transfers were calculated between −0.039 and −0.074 e$^-$, see Table S2. These values indicate that the adsorbate loses electronic density to the heterojunction functionalised with the nanocluster, showing no clear correlation with the binding energies of the VOC and H$_2$ molecules. The small values of electron density flow that we have calculated for this material support the low sensitivity that it displayed in the experiments.

Figure S15g-i depicts the structures of the molecular interactions with the surface sites of the heteroepitaxial material decorated with Ag$_6$Pt that released the largest adsorption energies. We found that H$_2$ remained perpendicularly atop the axial Pt atom at 1.91 Å,

27

while it coordinated laterally the equatorial Ag site at the more elongated distance of 2.07 Å, which moved outwards upon adsorption, see Figure S15g. Our DFT modelling suggests that C_2H_5OH prefers to stay parallel to the surface, binding both adsorption sites at the same distance of 2.29 Å, regardless of the different chemical nature of the metal atom, as shown in Figure S15h. When n-C_4H_9OH interacts with the axial or equatorial adsorption sites, the large alkyl radical positions itself perpendicularly to the surface. Figure 9c illustrates that n-C_4H_9OH has a bidentate coordination mode with $Ag_6Pt/TiO_2(111)/CuO(\bar{1}11)/Cu_2O(111)$, by binding laterally to the equatorial Ag atom and by forming a hydrogen bond between the hydroxyl H and one of the surface O species. Moving this alcohol to the axial site forces a reduction of the interfacial O−Pt distance to 2.23 Å, which is nevertheless insufficient to counteract the loss of the hydrogen bond formed on the equatorial Ag site.

Our calculated charge transfers indicate that most of the adsorbates donate electron density to the sensor containing the Ag_6Pt nanoclusters, see Table S2. The electronic charges transferred by C_2H_5OH to the axial and equatorial sites of the nanoparticle are −0.085 and −0.098 e⁻, respectively, displaying a direct correlation with the adsorption energies released in these positions. In contrast, n-C_4H_9OH donated −0.065 e⁻ in the most stable adsorption configuration on Ag_6Pt, a value that nearly doubled in the axial Pt position, leading to the largest charge transfer on this sensor. Despite H_2 having very close binding energies on both adsorption sites of Ag_6Pt, our models suggest that those interactions cause opposite flows of electron density, with the molecule receiving a charge of 0.011 e⁻ in the axial position. The density of states (DOS) are provided in Figure S16 to validate the stability of the system.

A discussion of the adsorption geometries and charge transfers for the least favourable interactions can be found in the Text S4 (Supporting Information).

4. Conclusion

Changing the composition of the nanolayered CuO/Cu_2O structure with a total thickness of 60 nm by first depositing 20 nm of TiO_2 on top and subsequently Ag nanoparticles (5-15 nm of diameter), reduces the energy consumption of the final gas sensing device to

28

below 1 nW. This fabrication process also allows tuning of the response spectrum of the sensor, thereby promoting the selectivity to 100 ppm of *n*-butanol vapours (response of over 200% at the operating temperature of 300°C). In the case of AgPt functionalization, the response of the sensor increases even further to 220% for 100 ppm of *n*-butanol vapours at an operating temperature of 350°C. In the case of Pd functionalization the selectivity of the sensor was changed from ethanol to hydrogen H_2, and the sensing performance was enhanced compared to the other compounds (response in the range between 400-600% at the lower operating temperature of 150-250°C).

A tentative surface reaction mechanism explaining the sensing behavior is proposed. At the interface of the TiO_2/CuO/Cu_2O heterostructure, the ethanol molecule first suffers a reduction and is then combined with the holes present in CuO, producing the CH_3CHO intermediate, which finally reacts with the oxygen adsorbed on the *n-type* TiO_2 overlayer. We have used thermodynamic arguments derived from DFT calculations to rationalize the stability of the heteroepitaxial material before and after surface functionalization by noble metal nanoparticles. The adsorption energies agree and support the gas sensing experiments. This manuscript presents the methodology for nano-structuring and functionalizing of semiconducting oxides with tunable performances, as an alternative to clean room technology and micro-fabrication.

29

References

[1] F. Rasch, V. Postica, F. Schütt, Y.K. Mishra, A.S. Nia, M.R. Lohe, X. Feng, R. Adelung, O. Lupan, Highly selective and ultra-low power consumption metal oxide based hydrogen gas sensor employing graphene oxide as molecular sieve, Sensors Actuators B Chem. 320 (2020) 128363. https://doi.org/10.1016/j.snb.2020.128363.

[2] F. Xue, L. Yang, M. Chen, J. Chen, X. Yang, L. Wang, L. Chen, C. Pan, Z.L. Wang, Enhanced photoresponsivity of the MoS_2-GaN heterojunction diode via the piezo-phototronic effect, NPG Asia Mater. 9 (2017) e418–e418. https://doi.org/10.1038/am.2017.142.

[3] D. Zappa, V. Galstyan, N. Kaur, H.M.M. Munasinghe Arachchige, O. Sisman, E. Comini, "Metal oxide -based heterostructures for gas sensors"- A review, Anal. Chim. Acta. 1039 (2018) 1–23. https://doi.org/10.1016/j.aca.2018.09.020.

[4] M. Hoppe, N. Ababii, V. Postica, O. Lupan, O. Polonskyi, F. Schütt, S. Kaps, L.F. Sukhodub, V. Sontea, T. Strunskus, F. Faupel, R. Adelung, (CuO-Cu_2O)/ZnO:Al heterojunctions for volatile organic compound detection, Sensors Actuators B Chem. 255 (2018) 1362–1375. https://doi.org/10.1016/j.snb.2017.08.135.

[5] S.M. Majhi, A. Mirzaei, H.W. Kim, S.S. Kim, T.W. Kim, Recent advances in energy-saving chemiresistive gas sensors: A review, Nano Energy. 79 (2021) 105369. https://doi.org/10.1016/j.nanoen.2020.105369.

[6] J.-H. Kim, P. Wu, H.W. Kim, S.S. Kim, Highly Selective Sensing of CO, C_6H_6, and C_7H_8 Gases by Catalytic Functionalization with Metal Nanoparticles, ACS Appl. Mater. Interfaces. 8 (2016) 7173–7183. https://doi.org/10.1021/acsami.6b01116.

[7] N. Ababii, M. Hoppe, S. Shree, A. Vahl, M. Ulfa, T. Pauporté, B. Viana, V. Cretu, N. Magariu, V. Postica, V. Sontea, M.-I. Terasa, O. Polonskyi, F. Faupel, R. Adelung, O. Lupan, Effect of noble metal functionalization and film thickness on sensing properties of sprayed TiO_2 ultra-thin films, Sensors Actuators A Phys. 293 (2019) 242–258. https://doi.org/10.1016/j.sna.2019.04.017.

[8] A. Vahl, J. Dittmann, J. Jetter, S. Veziroglu, S. Shree, N. Ababii, O. Lupan, O.C.

Aktas, T. Strunskus, E. Quandt, R. Adelung, S.K. Sharma, F. Faupel, The impact of O_2/Ar ratio on morphology and functional properties in reactive sputtering of metal oxide thin films, Nanotechnology. 30 (2019) 235603. https://doi.org/10.1088/1361-6528/ab0837.

[9]   V. Postica, A. Vahl, D. Santos-Carballal, T. Dankwort, L. Kienle, M. Hoppe, A. Cadi-Essadek, N.H. de Leeuw, M.-I. Terasa, R. Adelung, F. Faupel, O. Lupan, Tuning ZnO Sensors Reactivity toward Volatile Organic Compounds via Ag Doping and Nanoparticle Functionalization, ACS Appl. Mater. Interfaces. 11 (2019) 31452–31466. https://doi.org/10.1021/acsami.9b07275.

[10] G. Niu, C. Zhao, H. Gong, Z. Yang, X. Leng, F. Wang, NiO nanoparticle-decorated SnO_2 nanosheets for ethanol sensing with enhanced moisture resistance, Microsystems Nanoeng. 5 (2019) 21. https://doi.org/10.1038/s41378-019-0060-7.

[11] A. Vahl, O. Lupan, D. Santos-Carballal, V. Postica, S. Hansen, H. Cavers, N. Wolff, M.-I. Terasa, M. Hoppe, A. Cadi-Essadek, T. Dankwort, L. Kienle, N.H. de Leeuw, R. Adelung, F. Faupel, Surface functionalization of ZnO:Ag columnar thin films with AgAu and AgPt bimetallic alloy nanoparticles as an efficient pathway for highly sensitive gas discrimination and early hazard detection in batteries, J. Mater. Chem. A. 8 (2020) 16246–16264. https://doi.org/10.1039/D0TA03224G.

[12] H. Liu, W. Shen, X. Chen, A room temperature operated ammonia gas sensor based on Ag-decorated TiO_2 quantum dot clusters, RSC Adv. 9 (2019) 24519–24526. https://doi.org/10.1039/C9RA05439A.

[13] D. Zhao, M. Dai, Y. Zhao, H. Liu, Y. Liu, X. Wu, Improving electrocatalytic activities of $FeCo_2O_4$@$FeCo_2S_4$@PPy electrodes by surface/interface regulation, Nano Energy. 72 (2020) 104715. https://doi.org/10.1016/j.nanoen.2020.104715.

[14] D. Zhao, H. Liu, X. Wu, Bi-interface induced multi-active MCo_2O_4@MCo_2S_4@PPy (M=Ni, Zn) sandwich structure for energy storage and electrocatalysis, Nano Energy. 57 (2019) 363–370. https://doi.org/10.1016/j.nanoen.2018.12.066.

[15] D. Zhao, M. Dai, H. Liu, K. Chen, X. Zhu, D. Xue, X. Wu, J. Liu, Sulfur-Induced Interface Engineering of Hybrid $NiCo_2O_4$@$NiMo_2S_4$ Structure for Overall Water

Splitting and Flexible Hybrid Energy Storage, Adv. Mater. Interfaces. 6 (2019) 1901308. https://doi.org/10.1002/admi.201901308.

[16]   H. Liu, D. Zhao, Y. Liu, P. Hu, X. Wu, H. Xia, Boosting energy storage and electrocatalytic performances by synergizing $CoMoO_4$@$MoZn_{22}$ core-shell structures, Chem. Eng. J. 373 (2019) 485–492. https://doi.org/10.1016/j.cej.2019.05.066.

[17]   H. Wang, Y. Qu, H. Chen, Z. Lin, K. Dai, Highly selective n-butanol gas sensor based on mesoporous SnO_2 prepared with hydrothermal treatment, Sensors Actuators B Chem. 201 (2014) 153–159. https://doi.org/10.1016/j.snb.2014.04.049.

[18]   New Jersey Department of Health, Right to Know Hazardous Substance Fact Sheet - n-butyl alcohol, (2008). https://www.nj.gov/health/eoh/rtkweb/documents/fs/1330.pdf (accessed January 15, 2020).

[19]   I.S. Maddox, Production of n-butanol from whey filtrate using clostridium acetobutylicum N.C.I.B. 2951, Biotechnol. Lett. 2 (1980) 493–498. https://doi.org/10.1007/BF00129545.

[20]   C.-L. Cheng, P.-Y. Che, B.-Y. Chen, W.-J. Lee, L.-J. Chien, J.-S. Chang, High yield bio-butanol production by solvent-producing bacterial microflora, Bioresour. Technol. 113 (2012) 58–64. https://doi.org/10.1016/j.biortech.2011.12.133.

[21]   J. Huang, Y. Wu, C. Gu, M. Zhai, K. Yu, M. Yang, J. Liu, Large-scale synthesis of flowerlike ZnO nanostructure by a simple chemical solution route and its gas-sensing property, Sensors Actuators B Chem. 146 (2010) 206–212. https://doi.org/10.1016/j.snb.2010.02.052.

[22]   O. Lupan, V. Cretu, V. Postica, N. Ababii, O. Polonskyi, V. Kaidas, F. Schütt, Y.K. Mishra, E. Monaico, I. Tiginyanu, V. Sontea, T. Strunskus, F. Faupel, R. Adelung, Enhanced ethanol vapour sensing performances of copper oxide nanocrystals with mixed phases, Sensors Actuators B Chem. 224 (2016) 434–448. https://doi.org/10.1016/j.snb.2015.10.042.

[23]   V. Cretu, V. Postica, A.K. Mishra, M. Hoppe, I. Tiginyanu, Y.K. Mishra, L. Chow,

N.H. de Leeuw, R. Adelung, O. Lupan, Synthesis, characterization and DFT studies of zinc-doped copper oxide nanocrystals for gas sensing applications, J. Mater. Chem. A. 4 (2016) 6527–6539. https://doi.org/10.1039/C6TA01355D.

[24] L.-J. Zhou, Y.-C. Zou, J. Zhao, P.-P. Wang, L.-L. Feng, L.-W. Sun, D.-J. Wang, G.-D. Li, Facile synthesis of highly stable and porous Cu_2O/CuO cubes with enhanced gas sensing properties, Sensors Actuators B Chem. 188 (2013) 533–539. https://doi.org/10.1016/j.snb.2013.07.059.

[25] H. Haberland, M. Karrais, M. Mall, Y. Thurner, Thin films from energetic cluster impact: A feasibility study, J. Vac. Sci. Technol. A Vacuum, Surfaces, Film. 10 (1992) 3266–3271. https://doi.org/10.1116/1.577853.

[26] A. Vahl, J. Strobel, W. Reichstein, O. Polonskyi, T. Strunskus, L. Kienle, F. Faupel, Single target sputter deposition of alloy nanoparticles with adjustable composition via a gas aggregation cluster source, Nanotechnology. 28 (2017) 175703. https://doi.org/10.1088/1361-6528/aa66ef.

[27] S. Veziroglu, J. Hwang, J. Drewes, I. Barg, J. Shondo, T. Strunskus, O. Polonskyi, F. Faupel, O.C. Aktas, PdO nanoparticles decorated TiO_2 film with enhanced photocatalytic and self-cleaning properties, Mater. Today Chem. 16 (2020) 100251. https://doi.org/10.1016/j.mtchem.2020.100251.

[28] O. Lupan, V. Postica, M. Hoppe, N. Wolff, O. Polonskyi, T. Pauporté, B. Viana, O. Majérus, L. Kienle, F. Faupel, R. Adelung, PdO/PdO_2 functionalized ZnO:Pd films for lower operating temperature H_2 gas sensing, Nanoscale. 10 (2018) 14107–14127. https://doi.org/10.1039/C8NR03260B.

[29] O. Lupan, V. Cretu, V. Postica, O. Polonskyi, N. Ababii, F. Schütt, V. Kaidas, F. Faupel, R. Adelung, Non-planar nanoscale p–p heterojunctions formation in $Zn_xCu_{1-x}O_y$ nanocrystals by mixed phases for enhanced sensors, Sensors Actuators B Chem. 230 (2016) 832–843. https://doi.org/10.1016/j.snb.2016.02.089.

[30] G. Kresse, J. Hafner, Ab initio molecular dynamics for liquid metals, Phys. Rev. B. 47 (1993) 558–561. https://doi.org/10.1103/PhysRevB.47.558.

[31] G. Kresse, J. Hafner, Ab initio molecular-dynamics simulation of the liquid-metal–amorphous-semiconductor transition in germanium, Phys. Rev. B. 49 (1994)

34

14251–14269. https://doi.org/10.1103/PhysRevB.49.14251.

[32] G. Kresse, J. Furthmüller, Efficient iterative schemes for ab initio total-energy calculations using a plane-wave basis set, Phys. Rev. B. 54 (1996) 11169–11186. https://doi.org/10.1103/PhysRevB.54.11169.

[33] G. Kresse, J. Furthmüller, Efficiency of ab-initio total energy calculations for metals and semiconductors using a plane-wave basis set, Comput. Mater. Sci. 6 (1996) 15–50. https://doi.org/10.1016/0927-0256(96)00008-0.

[34] J.P. Perdew, K. Burke, M. Ernzerhof, Generalized Gradient Approximation Made Simple [Phys. Rev. Lett. 77, 3865 (1996)], Phys. Rev. Lett. 78 (1997) 1396–1396. https://doi.org/10.1103/PhysRevLett.78.1396.

[35] J.P. Perdew, K. Burke, M. Ernzerhof, Generalized Gradient Approximation Made Simple, Phys. Rev. Lett. 77 (1996) 3865–3868. https://doi.org/10.1103/PhysRevLett.77.3865.

[36] S. Grimme, J. Antony, S. Ehrlich, H. Krieg, A consistent and accurate ab initio parametrization of density functional dispersion correction (DFT-D) for the 94 elements H-Pu., J. Chem. Phys. 132 (2010) 154104. https://doi.org/10.1063/1.3382344.

[37] S. Grimme, S. Ehrlich, L. Goerigk, Effect of the damping function in dispersion corrected density functional theory., J. Comput. Chem. 32 (2011) 1456–1465. https://doi.org/10.1002/jcc.21759.

[38] B. Farkaš, D. Santos-Carballal, A. Cadi-Essadek, N.H. de Leeuw, A DFT+U study of the oxidation of cobalt nanoparticles: Implications for biomedical applications, Materialia. 7 (2019) 100381. https://doi.org/10.1016/j.mtla.2019.100381.

[39] M.J. Ungerer, D. Santos-Carballal, A. Cadi-Essadek, C.G.C.E. van Sittert, N.H. de Leeuw, Interaction of H_2O with the Platinum Pt (001), (011), and (111) Surfaces: A Density Functional Theory Study with Long-Range Dispersion Corrections, J. Phys. Chem. C. 123 (2019) 27465–27476. https://doi.org/10.1021/acs.jpcc.9b06136.

[40] L.M. Botha, D. Santos-Carballal, U. Terranova, M.G. Quesne, M.J. Ungerer, C.G.C.E. van Sittert, N.H. de Leeuw, Mixing thermodynamics and electronic

structure of the $Pt_{1-x}Ni_x$ ($0 \leq x \leq 1$) bimetallic alloy, RSC Adv. 9 (2019) 16948–16954. https://doi.org/10.1039/C9RA02320H.

[41] D. Santos-Carballal, P.E. Ngoepe, N.H. de Leeuw, Ab initio investigation of the thermodynamics of cation distribution and of the electronic and magnetic structures in the $LiMn_2O_4$ spinel, Phys. Rev. B. 97 (2018) 085126. https://doi.org/10.1103/PhysRevB.97.085126.

[42] S. Posada-Pérez, D. Santos-Carballal, U. Terranova, A. Roldan, F. Illas, N.H. de Leeuw, CO_2 Interaction with Violarite ($FeNi_2S_4$) Surfaces: A Dispersion-Corrected DFT Study, Phys. Chem. Chem. Phys. 20 (2018) 20439–20446. https://doi.org/10.1039/C8CP03430C.

[43] V. Postica, A. Vahl, J. Strobel, D. Santos-Carballal, O. Lupan, A. Cadi-Essadek, N.H. De Leeuw, F. Schütt, O. Polonskyi, T. Strunskus, M. Baum, L. Kienle, R. Adelung, F. Faupel, Tuning doping and surface functionalization of columnar oxide films for volatile organic compounds sensing: Experiments and theory, J. Mater. Chem. A. 6 (2018) 23669–23682. https://doi.org/10.1039/C8TA08985J.

[44] L. Reguera, N.L. López, J. Rodríguez-Hernández, M. González, C.E. Hernandez-Tamargo, D. Santos-Carballal, N.H. de Leeuw, E. Reguera, Synthesis, Crystal Structures, and Properties of Zeolite-Like $T_3(H_3O)_2M(CN)_6]_2 \cdot uH_2O$ (T = Co, Zn; M = Ru, Os), Eur. J. Inorg. Chem. 2017 (2017) 2980–2989. https://doi.org/10.1002/ejic.201700278.

[45] B. Ramogayana, D. Santos-Carballal, P.A. Aparicio, M.G. Quesne, K.P. Maenetja, P.E. Ngoepe, N.H. de Leeuw, Ethylene carbonate adsorption on the major surfaces of lithium manganese oxide $Li_{1-x}Mn_2O_4$ spinel ($0.000 < x < 0.375$): a DFT+ U -D3 study, Phys. Chem. Chem. Phys. 22 (2020) 6763–6771. https://doi.org/10.1039/C9CP05658K.

[46] P.E. Blöchl, Projector augmented-wave method, Phys. Rev. B. 50 (1994) 17953–17979. https://doi.org/10.1103/PhysRevB.50.17953.

[47] G. Kresse, D. Joubert, From ultrasoft pseudopotentials to the projector augmented-wave method, Phys. Rev. B. 59 (1999) 1758–1775. https://doi.org/10.1103/PhysRevB.59.1758.

[48] D. Sheppard, R. Terrell, G. Henkelman, Optimization methods for finding minimum energy paths., J. Chem. Phys. 128 (2008) 134106. https://doi.org/10.1063/1.2841941.

[49] M.R. Hestenes, E. Stiefel, Methods of conjugate gradients for solving linear systems, J. Res. Natl. Bur. Stand. 49 (1952) 409. https://doi.org/10.6028/jres.049.044.

[50] V.I. Anisimov, M.A. Korotin, J. Zaanen, O.K. Andersen, Spin bags, polarons, and impurity potentials in $La_{2-x}Sr_xCuO_4$ from first principles, Phys. Rev. Lett. 68 (1992) 345–348. https://doi.org/10.1103/PhysRevLett.68.345.

[51] S.L. Dudarev, G.A. Botton, S.Y. Savrasov, C.J. Humphreys, A.P. Sutton, Electron-energy-loss spectra and the structural stability of nickel oxide: An LSDA+U study, Phys. Rev. B. 57 (1998) 1505–1509. https://doi.org/10.1103/PhysRevB.57.1505.

[52] I. de P.R. Moreira, F. Illas, R.L. Martin, Effect of Fock exchange on the electronic structure and magnetic coupling in NiO, Phys. Rev. B. 65 (2002) 155102. https://doi.org/10.1103/PhysRevB.65.155102.

[53] C.E. Calderon, J.J. Plata, C. Toher, C. Oses, O. Levy, M. Fornari, A. Natan, M.J. Mehl, G. Hart, M. Buongiorno Nardelli, S. Curtarolo, The AFLOW standard for high-throughput materials science calculations, Comput. Mater. Sci. 108 (2015) 233–238. https://doi.org/10.1016/j.commatsci.2015.07.019.

[54] W. Setyawan, S. Curtarolo, High-throughput electronic band structure calculations: Challenges and tools, Comput. Mater. Sci. 49 (2010) 299–312. https://doi.org/10.1016/j.commatsci.2010.05.010.

[55] W. Setyawan, R.M. Gaume, S. Lam, R.S. Feigelson, S. Curtarolo, High-throughput combinatorial database of electronic band structures for inorganic scintillator materials, ACS Comb. Sci. 13 (2011) 382–390. https://doi.org/10.1021/co200012w.

[56] S. Wang, Z. Wang, W. Setyawan, N. Mingo, S. Curtarolo, Assessing the Thermoelectric Properties of Sintered Compounds via High-Throughput Ab-Initio Calculations, Phys. Rev. X. 1 (2011) 1–8. https://doi.org/10.1103/PhysRevX.1.021012.

[57] R.H. Taylor, F. Rose, C. Toher, O. Levy, K. Yang, M. Buongiorno Nardelli, S. Curtarolo, A RESTful API for exchanging materials data in the AFLOWLIB.org consortium, Comput. Mater. Sci. 93 (2014) 178–192. https://doi.org/10.1016/j.commatsci.2014.05.014.

[58] O.K. Andersen, Electronic structure of the fcc transition metals Ir, Rh, Pt, and Pd, Phys. Rev. B. 2 (1970) 883–906. https://doi.org/10.1103/PhysRevB.2.883.

[59] W. Speier, J.C. Fuggle, R. Zeller, B. Ackermann, K. Szot, F.U. Hillebrecht, M. Campagna, Bremsstrahlung isochromat spectra and density-of-states calculations for the 3d and 4d transition metals, Phys. Rev. B. 30 (1984) 6921–6930. https://doi.org/10.1103/PhysRevB.30.6921.

[60] H.J. Monkhorst, J.D. Pack, Special points for Brillouin-zone integrations, Phys. Rev. B. 13 (1976) 5188–5192. https://doi.org/10.1103/PhysRevB.13.5188.

[61] M. Methfessel, A.T. Paxton, High-precision sampling for Brillouin-zone integration in metals, Phys. Rev. B. 40 (1989) 3616–3621. https://doi.org/10.1103/PhysRevB.40.3616.

[62] N.D. Mermin, Thermal Properties of the Inhomogeneous Electron Gas, Phys. Rev. 137 (1965) A1441–A1443. https://doi.org/10.1103/PhysRev.137.A1441.

[63] P.E. Blöchl, O. Jepsen, O.K. Andersen, Improved tetrahedron method for Brillouin-zone integrations, Phys. Rev. B. 49 (1994) 16223–16233. https://doi.org/10.1103/PhysRevB.49.16223.

[64] W. Li, X. Yan, A.G. Aberle, S. Venkataraj, Effect of sodium diffusion on the properties of CIGS solar absorbers prepared using elemental Se in a two-step process, Sci. Rep. 9 (2019) 2637. https://doi.org/10.1038/s41598-019-39283-2.

[65] J.-T. Fonné, E. Burov, E. Gouillart, S. Grachev, H. Montigaud, D. Vandembroucq, Interdiffusion between silica thin films and soda-lime glass substrate during annealing at high temperature, J. Am. Ceram. Soc. 102 (2019) 3341–3353. https://doi.org/10.1111/jace.16154.

[66] J.F. Moulder, W.F. Stickle, P.E. Sobol, K.D. Bomben, Handbook of X-ray Photoelectron Spectroscopy, Perkin-Elmer Corporation, Eden Prairie, Minnesota, 1992. https://www.cnyn.unam.mx/~wencel/XPS/MANXPS.pdf.

[67] C.J.P. Alexander V. Naumkin, Anna Kraut-Vass, Stephen W. Gaarenstroom, NIST X-ray Photoelectron Spectroscopy Database, NIST X-Ray Photoelectron Spectrosc. Database, NIST Stand. Ref. Database 20, Version 4.1. (2000). https://doi.org/10.18434/T4T88K.

[68] A. Sahai, N. Goswami, S.D. Kaushik, S. Tripathi, $Cu/Cu_2O/CuO$ nanoparticles: Novel synthesis by exploding wire technique and extensive characterization, Appl. Surf. Sci. 390 (2016) 974–983. https://doi.org/10.1016/j.apsusc.2016.09.005.

[69] K.A. Willets, R.P. Van Duyne, Localized Surface Plasmon Resonance Spectroscopy and Sensing, Annu. Rev. Phys. Chem. 58 (2007) 267–297. https://doi.org/10.1146/annurev.physchem.58.032806.104607.

[70] J.R. Ferraro, K. Nakamoto, Basic Theory, in: J.R. Ferraro, K.B.T.-I.R.S. Nakamoto (Eds.), Introd. Raman Spectrosc., Elsevier, Boston, 1994: pp. 1–94. https://doi.org/10.1016/B978-0-12-253990-9.50005-7.

[71] C.K. Law, Resonance Response of the Quantum Vacuum to an Oscillating Boundary, Phys. Rev. Lett. 73 (1994) 1931–1934. https://doi.org/10.1103/PhysRevLett.73.1931.

[72] F. Wooten, Optical properties of solids, Academic Press, New York, NY, 1972. http://cds.cern.ch/record/268948.

[73] A.E. Rakhshani, Preparation, characteristics and photovoltaic properties of cuprous oxide—a review, Solid. State. Electron. 29 (1986) 7–17. https://doi.org/10.1016/0038-1101(86)90191-7.

[74] B. Balamurugan, I. Aruna, B.R. Mehta, S.M. Shivaprasad, Size-dependent conductivity-type inversion in Cu_2O nanoparticles, Phys. Rev. B. 69 (2004) 165419. https://doi.org/10.1103/PhysRevB.69.165419.

[75] V. Postica, A. Vahl, N. Magariu, M.-I. Terasa, M. Hoppe, B. Viana, P. Aschehoug, T. Pauporté, I. Tiginyanu, O. Polonskyi, V. Sontea, L. Chow, L. Kienle, R. Adelung, F. Faupel, O. Lupan, Enhancement in UV Sensing Properties of ZnO:Ag Nanostructured Films by Surface Functionalization with Noble Metalic and Bimetallic Nanoparticles, J. Eng. Sci. XXV (2018) 41–51. https://doi.org/10.5281/zenodo.2557280.

39

[76] M. Mathew, P. V Shinde, R. Samal, C.S. Rout, A review on mechanisms and recent developments in p-n heterojunctions of 2D materials for gas sensing applications, J. Mater. Sci. 56 (2021) 9575–9604. https://doi.org/10.1007/s10853-021-05884-4.

[77] H. Xuemei, S. Yukun, B. Bo, Fabrication of Cubic p-n Heterojunction-Like NiO/In$_2$O$_3$ Composite Microparticles and Their Enhanced Gas Sensing Characteristics, J. Nanomater. 2016 (2016) 1–9. https://doi.org/10.1155/2016/7589028.

[78] D.E.P. Vanpoucke, G. Brocks, Formation of Pt-induced Ge atomic nanowires on Pt/Ge(001): A density functional theory study, Phys. Rev. B. 77 (2008) 241308. https://doi.org/10.1103/PhysRevB.77.241308.

[79] J. Tersoff, D.R. Hamann, Theory of the scanning tunneling microscope, Phys. Rev. B. 31 (1985) 805–813. https://doi.org/10.1103/PhysRevB.31.805.